Supplementary Information for

Halide Segregation Governs Interfacial Charge-Transfer Pathways in Mixed-Halide Perovskites

Jae Eun Lee[1], Robert D. J. Oliver[2], Joshua R. S. Lilly[1], Rehmat Sood-Goodwin[3,4], Aleksander M Ulatowski,[1] Alexandra J. Ramadan[3], Henry J. Snaith[1], Michael B. Johnston[1] and Laura M. Herz[1,]*

Affiliations

[1] Department of Physics, University of Oxford, Clarendon Laboratory, Parks Road, Oxford, OX1 3PU, UK.

[2] Department of Physics and Astronomy, University of Sheffield, Hicks Building, Hounsfield Road, Sheffield, S37RH, UK.

[3] School of Mathematical and Physical Sciences, University of Sheffield, Hicks Building, Hounsfield Road, Sheffield, S3 7RH, UK.

[4] Grantham Centre for Sustainable Futures, University of Sheffield, Sheffield, S10 2TN, UK.

Corresponding Author

* E-mail: laura.herz@physics.ox.ac.uk

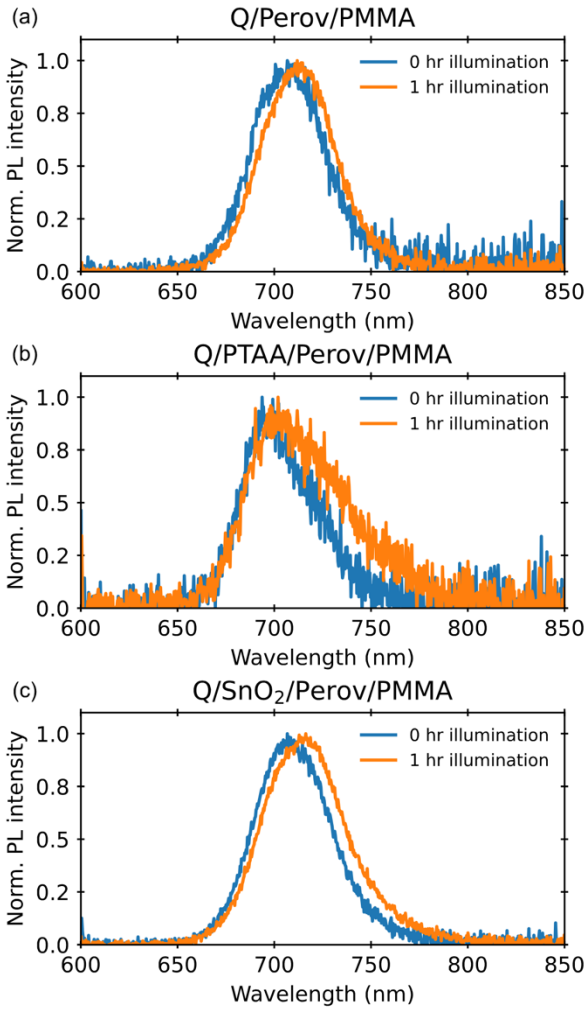

Fig. S1 Normalised steady-state photoluminescence (PL) of (a) Quartz(Q)/$FA_{0.83}Cs_{0.17}Pb(I_{0.6}Br_{0.4})_3$ (Perov)/PMMA, (b) Q/PTAA/Perov/PMMA and (c) Q/SnO_2/Perov/PMMA after 1 hr of continuous exposure to 530 nm pulsed excitation.

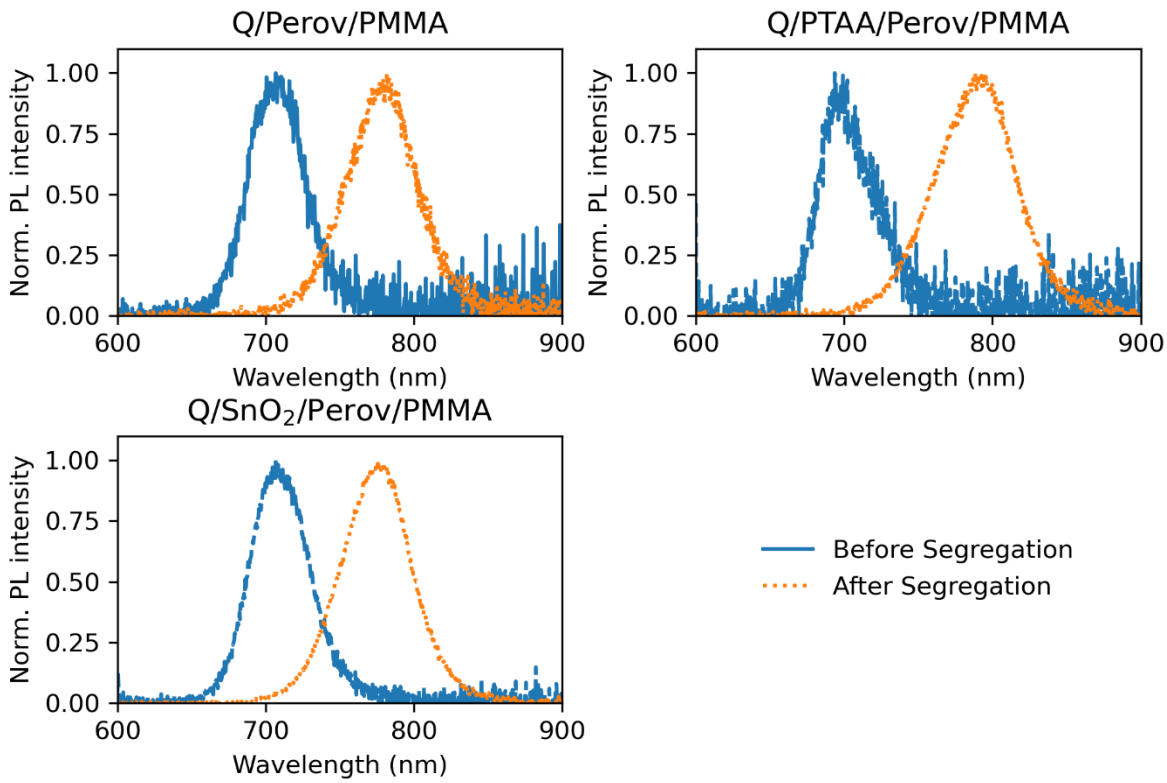

Fig. S2 Normalised steady-state photoluminescence (PL) of Quartz(Q)/$FA_{0.83}Cs_{0.17}Pb(I_{0.6}Br_{0.4})_3$ (Perov)/PMMA, Q/PTAA/Perov/PMMA and Q/SnO_2/Perov/PMMA before halide segregation (blue) and after halide segregation (orange).

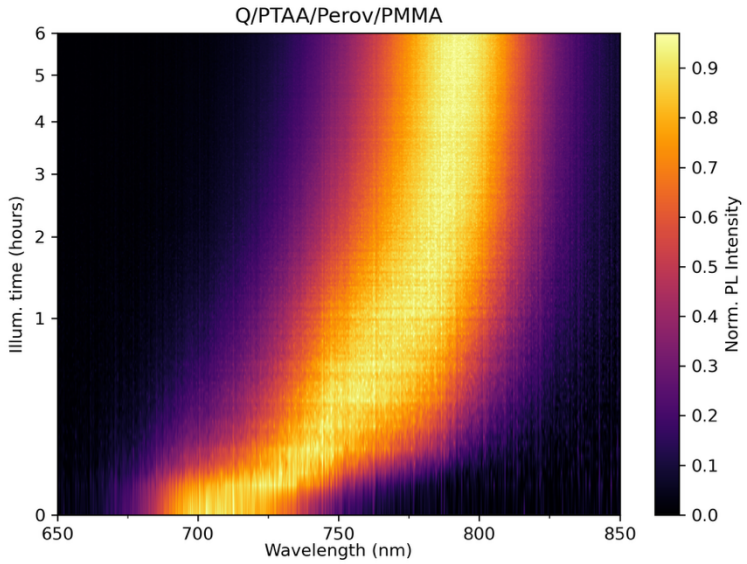

Fig. S3 Normalised steady-state PL contour map of Quartz(Q)/PTAA/$FA_{0.83}Cs_{0.17}Pb(I_{0.6}Br_{0.4})_3$ /PMMA recorded during 6 hours of CW illumination at the power density of 150 $mWcm^{-2}$. The illumination time is plotted on a square-root scale to highlight the early-time PL evolution.

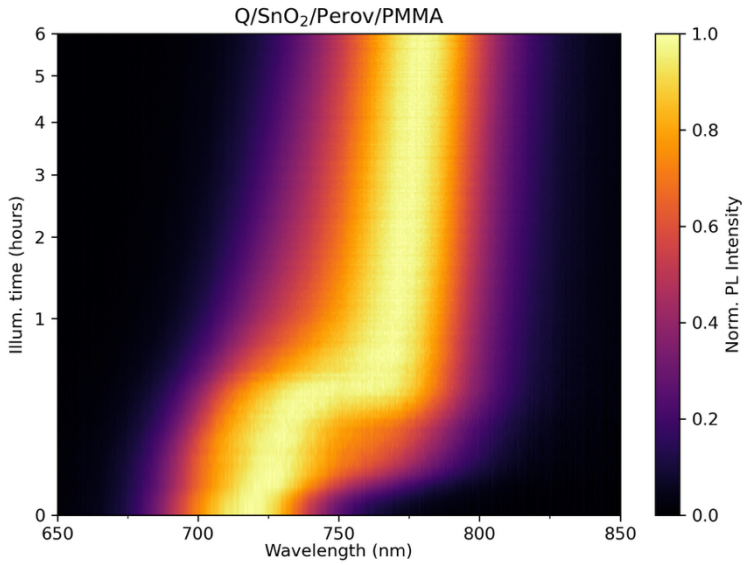

Fig. S4 Normalised steady-state PL contour map of Quartz(Q)/SnO_2/$FA_{0.83}Cs_{0.17}Pb(I_{0.6}Br_{0.4})_3$/ PMMA recorded during 6 hours of CW illumination at the power density of 150 $mWcm^{-2}$. The illumination time is plotted on a square-root scale to highlight the early-time PL evolution.

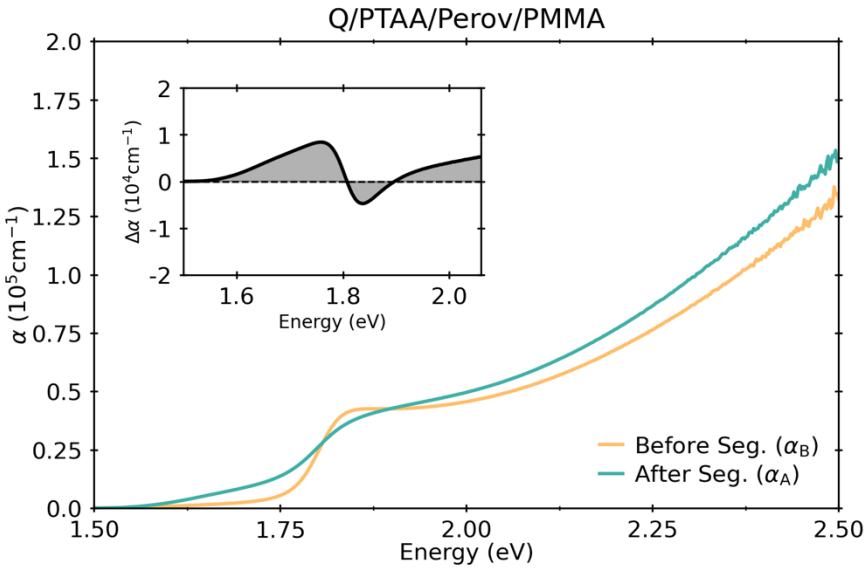

Fig. S5 Absorption spectra of Quartz(Q)/PTAA/$FA_{0.83}Cs_{0.17}Pb(I_{0.6}Br_{0.4})_3$/PMMA before ($\alpha_B$) and after halide segregation (α_A). The inset shows change in absorption spectra at ($\Delta\alpha = \alpha_A - \alpha_B$) at the absorption edge.

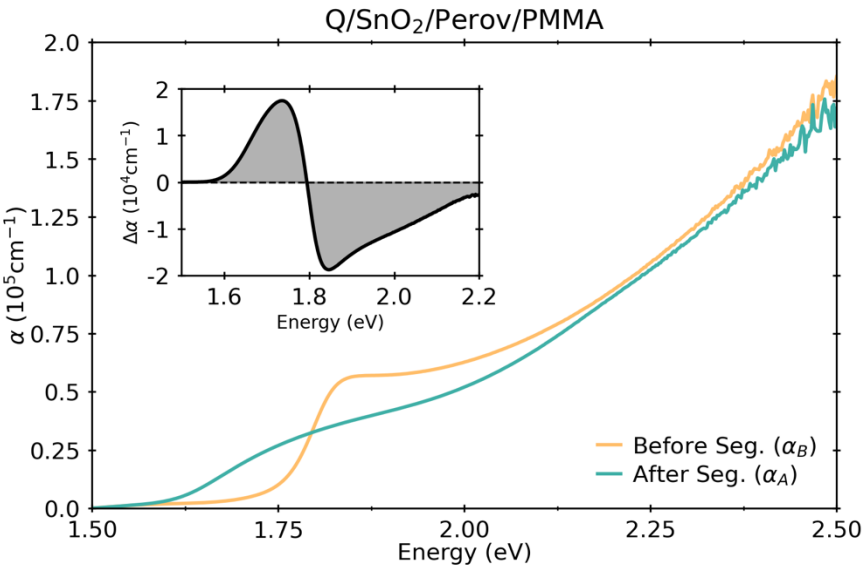

Fig. S6 Absorption spectra of Quartz(Q)/SnO_2/$FA_{0.83}Cs_{0.17}Pb(I_{0.6}Br_{0.4})_3$/PMMA before ($\alpha_B$) and after halide segregation (α_A). The inset shows change in absorption spectra at ($\Delta\alpha = \alpha_A - \alpha_B$) at the absorption edge.

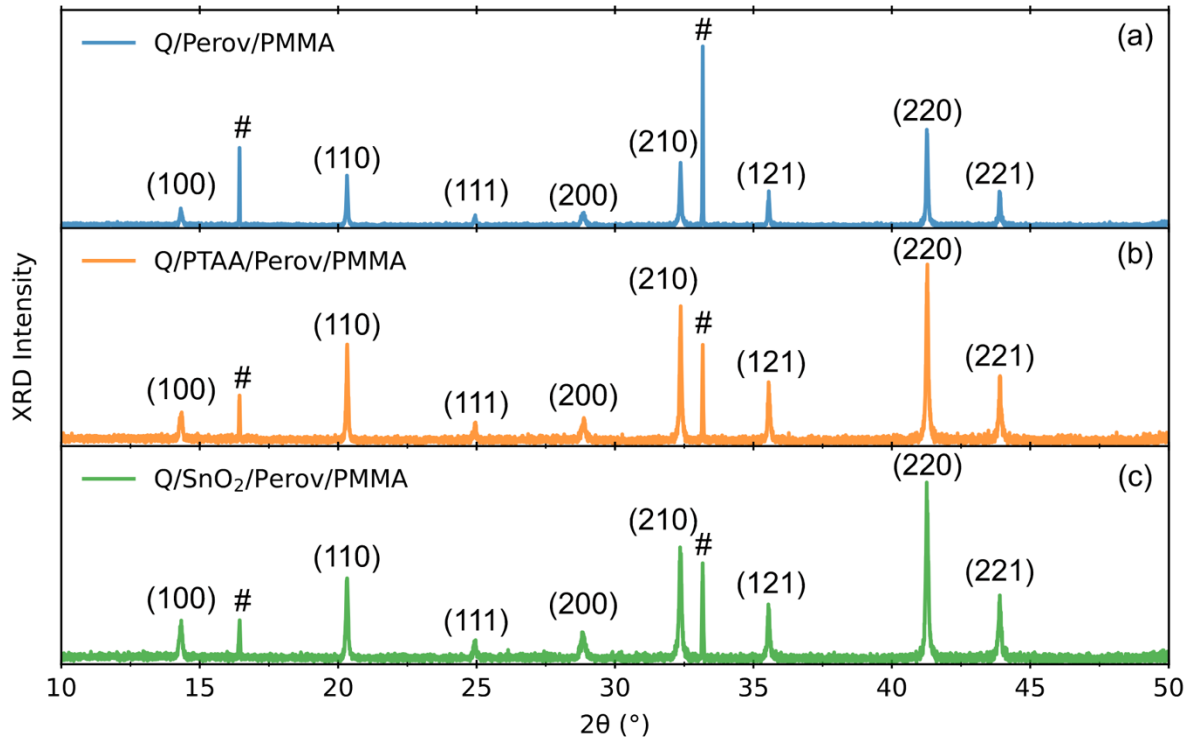

Fig. S7 XRD spectra of (a) Quartz(Q)/$FA_{0.83}Cs_{0.17}Pb(I_{0.6}Br_{0.4})_3$(Perov)/PMMA (blue), (b) Q/PTAA/Perov/PMMA (orange) and (c) Q/SnO_2/Perov/PMMA (green). Relevant pseudo-cubic peaks are labelled with the Miller indices and they are identical to the literature values.[1] The z-cut quartz reference peaks at 2θ = 16.433 ° and 33.172 ° are labelled as #.[2]

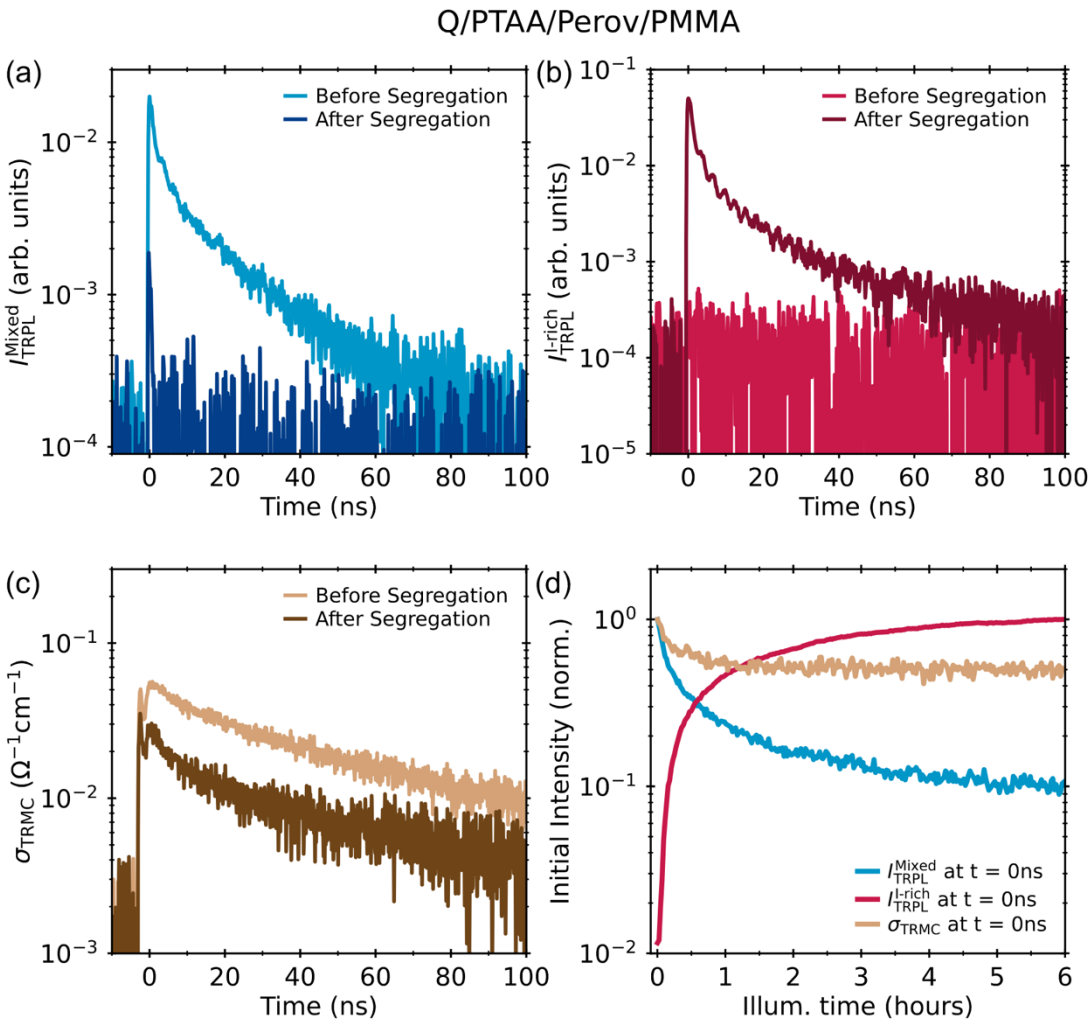

Fig. S8 Comparisons of Q/PTAA/Perov/PMMA transients. (a) Mixed-phase time-resolved photoluminescence (TRPL) I_{TRPL}^{Mixed} (658 ~ 694 nm) transient before and after halide segregation. (b) I-rich phase TRPL I_{TRPL}^{I-rich} (800 ~ 850 nm) transient before and after halide segregation. (c) Time-resolved microwave conductivity (σ_{TRMC}) transient before and after halide segregation. (d) Initial intensities of I_{TRPL}^{Mixed}, I_{TRPL}^{I-rich} and σ_{TRMC} at t = 0 ns as a function of illumination time.

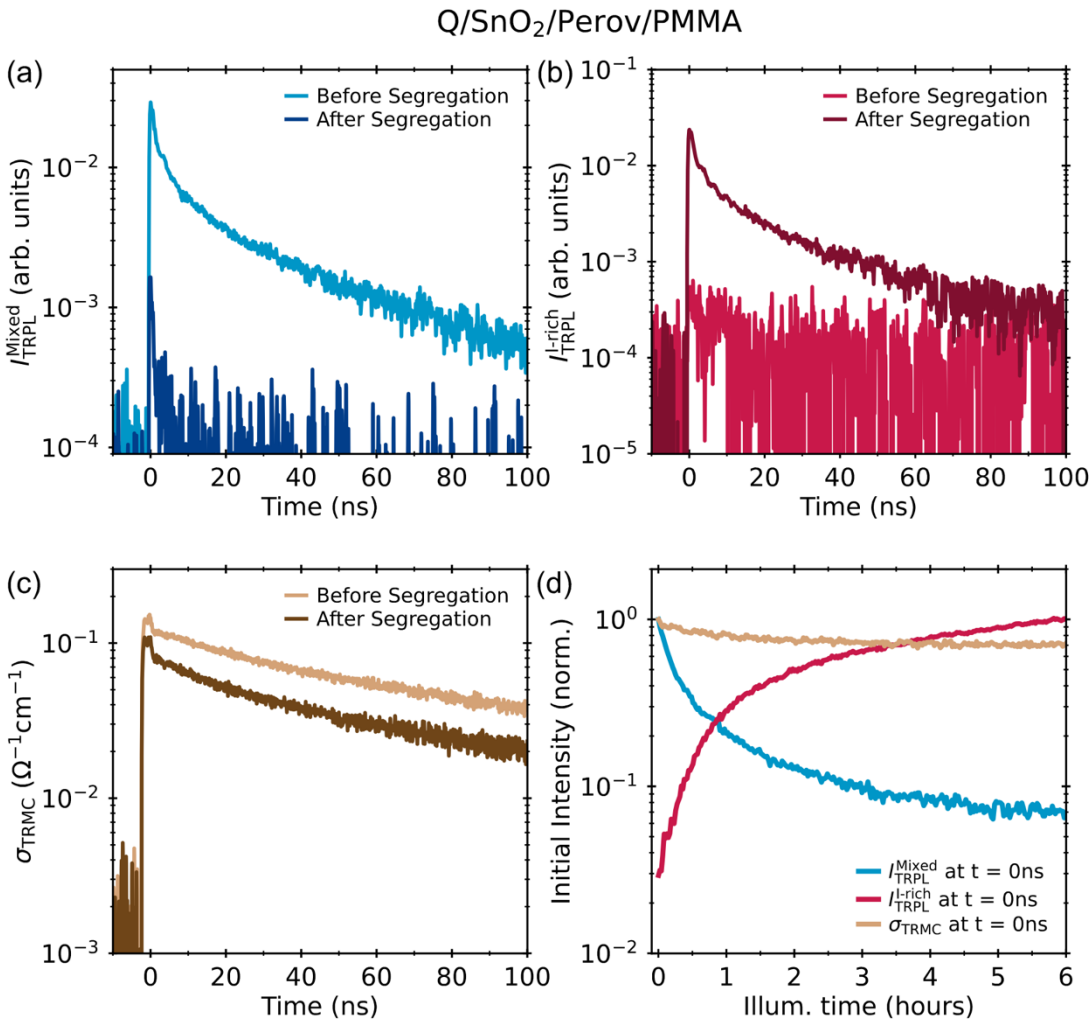

Fig. S9 Comparisons of Q/SnO_2/Perov/PMMA transients. (a) Mixed-phase time-resolved photoluminescence (TRPL) I_{TRPL}^{Mixed} (658 ~ 694 nm) transient before and after halide segregation. (b) I-rich phase TRPL I_{TRPL}^{I-rich} (800 ~ 850 nm) transient before and after halide segregation. (c) Time-resolved microwave conductivity (σ_{TRMC}) transient before and after halide segregation. (d) Initial intensities of I_{TRPL}^{Mixed}, I_{TRPL}^{I-rich} and σ_{TRMC} at t = 0 ns as a function of illumination time.

Table S1 Thickness of perovskite layer in each sample measured with Atomic Force Microscopy. AFM measurements were conducted using an MFP-3D Microscope (Asylum Research) and Scout RAl cantilevers. All image processing was conducted using Gwyddion (32bit).[3] For thickness measurements, a cantilever was mounted with spring constant of 41.52 N/m and resonant frequency of 318.79 kHz. Free amplitudes were ~50 nm, setpoints ~40 nm, and scan speeds of 6.25 um/s over an area of 25 um × 12.5 um. To find the thickness, line profiles across three different areas of images were taken and averaged. z-sensor channels were used to determine the thickness due to higher sensitivity. The thickness was determined pre-processing, as well as after plane level and line levelling and no differences were observed, showing the extracted thickness values were not affected by data processing protocol.

Samples	Perovskite layer thickness, d_{perov} (nm)
Q/Perov/PMMA	369
Q/PTAA/Perov/PMMA	407
Q/SnO_2/Perov/PMMA	336

Supplementary Note 1: Charge-carrier densities generated by pulsed excitation

The charge-carrier density is calculated by the following equation:

$$n_0 = \frac{F\lambda}{hcd_{\mathrm{perov}}}\left(1 - R_{\mathrm{pump}}(\lambda) - T_{\mathrm{pump}}(\lambda)\right) \quad \text{(S1)}$$

where F is the fluence of the optical excitation pulse of wavelength λ, h is the Planck constant, c is the speed of light, d_{perov} is the thickness of perovskite layer presented in Table S1. R_{pump} and T_{pump} are the sample reflectivity and transmittance at the pump wavelength λ.

Table S2 Charge-carrier density generated by 530 nm pulsed excitation at different fluences for TRPL and TRMC measurements.

Fluences (μJ cm^{-2})	Q/Perov/PMMA n_0 (10^{16} cm^{-3})	Q/PTAA/Perov/PMMA n_0 (10^{16} cm^{-3})	Q/SnO_2/Perov/PMMA n_0 (10^{16} cm^{-3})
0.3	1.8	1.5	1.9
0.4	2.9	2.5	3.2
1.4	9.1	8.0	10.1
3.6	24.2	21.2	26.8
7.9	52.9	46.4	58.7
16.3	108.7	95.4	120.7

Supplementary Note 2: Simulated transients in Figs. 1c and 1d.

For the simulated transients shown in Figs. 1c and 1d of the main text, we employ a charge-carrier trapping-detrapping model to illustrate the effect of charge-selective processes on the time-resolved photoluminescence intensity (I_{TRPL}), squared time-resolved photoconductivity (${\sigma_{\mathrm{TRMC}}}^2$) and the resulting ratio of $I_{\mathrm{TRPL}}/{\sigma_{\mathrm{TRMC}}}^2$.

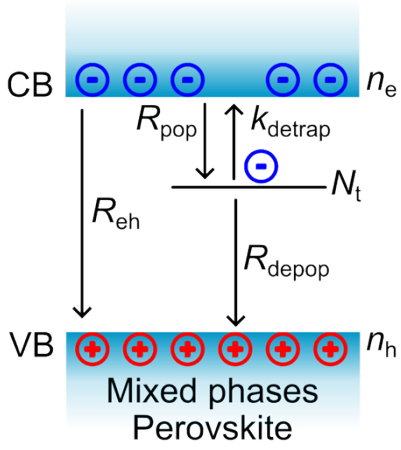

Fig. S10 Schematic illustration of the trap-mediated recombination model with recombination processes including radiative bimolecular recombination (R_{eh}), trap population (R_{pop}), depopulation (R_{depop}) and detrapping (k_{detrap}). CB and VB represent conduction band and valence band respectively. n_e, n_h, n_t and N_t correspond to electron density, hole density, trapped electron density and total trap density. The blue minus and red plus symbols denote electrons and holes in CB and VB respectively.

The schematic diagram in Fig. S10 summarises recombination processes included in the trap-mediated recombination model. Upon photoexcitation, electron-hole pairs are generated (blue minus and red plus symbols respectively) after which they can undergo either bimolecular radiative recombination with rate constant (R_{eh}), non-radiative trap-mediated recombination including trap population (R_{pop}), depopulation (R_{depop}) and detrapping (k_{detrap}). For demonstration purposes, we assume that electrons are preferentially trapped,[4-6] although we show in Supplementary Note 3 that it is not necessarily the case for mixed-halide perovskites. The temporal evolution of these processes is described by the following set of coupled differential equations:

$$\frac{dn_{\mathrm{e}}(t)}{dt} = -R_{\mathrm{eh}} n_{\mathrm{e}}(t) n_{\mathrm{h}}(t) - R_{\mathrm{pop}}(N_{\mathrm{t}} - n_{\mathrm{t}}(t)) n_{\mathrm{e}}(t) + k_{\mathrm{detrap}} n_{\mathrm{t}}(t) \quad \text{(S2)}$$

$$\frac{dn_{\mathrm{h}}(t)}{dt} = -R_{\mathrm{eh}} n_{\mathrm{e}}(t) n_{\mathrm{h}}(t) - R_{\mathrm{depop}} n_{\mathrm{t}}(t) n_{\mathrm{h}}(t) \quad \text{(S3)}$$

$$\frac{dn_{\mathrm{t}}(t)}{dt} = R_{\mathrm{pop}}(N_{\mathrm{t}} - n_{\mathrm{t}}(t)) n_{\mathrm{e}}(t) - R_{\mathrm{depop}} n_{\mathrm{t}}(t) n_{\mathrm{e}}(t) - k_{\mathrm{detrap}} n_{\mathrm{t}}(t) \quad \text{(S4)}$$

where $n_{\mathrm{e}}(t)$, $n_{\mathrm{h}}(t)$, $n_{\mathrm{t}}(t)$ and N_{t} are the electron density, hole density, trapped electron density and total trap density respectively.

The Equations S2, S3, and S4 were solved numerically to obtain $n_{\mathrm{e}}(t)$, $n_{\mathrm{h}}(t)$ and $n_{\mathrm{t}}(t)$,. Then, TRPL and TRMC transients are constructed by using the following relationships

$$I_{\mathrm{TRPL}} \propto R_{\mathrm{eh}} n_{\mathrm{e}}(t) n_{\mathrm{h}}(t) \quad \text{(S5)}$$

$$\sigma_{\mathrm{TRMC}} = e\mu(n_{\mathrm{e}}(t) + n_{\mathrm{h}}(t)) \quad \text{(S6)}$$

where μ is the charge-carrier mobility. Finally, the ratio of $I_{\mathrm{TRPL}}/{\sigma_{\mathrm{TRMC}}}^2$ is obtained by normalising both the I_{TRPL} and ${\sigma_{\mathrm{TRMC}}}^2$ transients to their initial values at t = 0 ns, and then taking the ratio. Here, we assume charge-carrier balance upon excitation and that traps are unfilled initially. For Figs. 1c and d in the main text, the parameters listed in Table S3 were used.

Table S3 Parameters used for the trap-mediated recombination model in Figs. 1c and 1d of the main text.

Parameters	Values	Reference
$n_{\mathrm{e}}(t=0)$ (cm^{-3})	2.42×10^{17}	Table S2
$n_{\mathrm{h}}(t=0)$ (cm^{-3})	2.42×10^{17}	
$n_{\mathrm{t}}(t=0)$ (cm^{-3})	0	-
μ (cm^{2}V^{-1}s^{-1})	24.5	Table S5
R_{eh} (cm^{3}s^{-1})	1.54×10^{-10}	Table S7
N_{t}(cm^{-3})	1.7×10^{15}	Ref. 1
R_{pop}(cm^{3}s^{-1})	9.5×10^{-9}	Ref. 1
R_{depop}(cm^{-3}s^{-1})	1.42×10^{-9}	Ref. 1
k_{detrap}(s^{-1})	5.6×10^{4}	Ref. 1

For Fig. 1d in main text, only N_{t} is increased to the value of 1×10^{17} cm^{-3} in order to make it comparable to the initial charge-carrier density, thereby allowing an assessment of the effects of dominant trap-mediated recombination.

The effect of charge-selective process (trap-mediated recombination here) is evident when observing the temporal evolution of charge-carriers under these recombination dynamics as shown in Fig. S11. When the trap density ($N_{\mathrm{t}} = 1 \times 10^{15}$ cm^{-3}) is orders of magnitude lower than the density of photogenerated charge carriers ($n_{\mathrm{e}}(0) = n_{\mathrm{h}}(0) = 2.42 \times 10^{17}$ cm^{-3}) (Fig. S11a), any initially available trap states are quickly saturated (populated). As a result, the density of free electrons is only slightly reduced and charge recombination is dominated by electron-hole bimolecular radiative processes. In contrast, when the trap density ($N_{\mathrm{t}} = 1 \times 10^{17}$ cm^{-3}) is comparable to the density of photogenerated charge carriers ($n_{\mathrm{e}}(0) = n_{\mathrm{h}}(0) = 2.42 \times 10^{17}$ cm^{-3}) (Fig. S11b), a substantial amount of electrons is depleted even at early times. This imbalance leaves behind holes which subsequently recombine with trapped electrons. Because trap depopulation occurs more slowly than trap population, long-lived holes persist and contribute to the σ_{TRMC} transient while I_{TRPL} is quenched, leading to the divergence in σ_{TRMC} and I_{TRPL} transients. Therefore, the model predicts that radiative recombination dominates when the trap density is significantly lower than the generated charge-carrier density by orders of magnitude. This condition can be generalised to operating solar cells, for which radiative recombination will prevail when the density of trap states remains well below the steady-state charge-carrier density under solar illumination conditions.

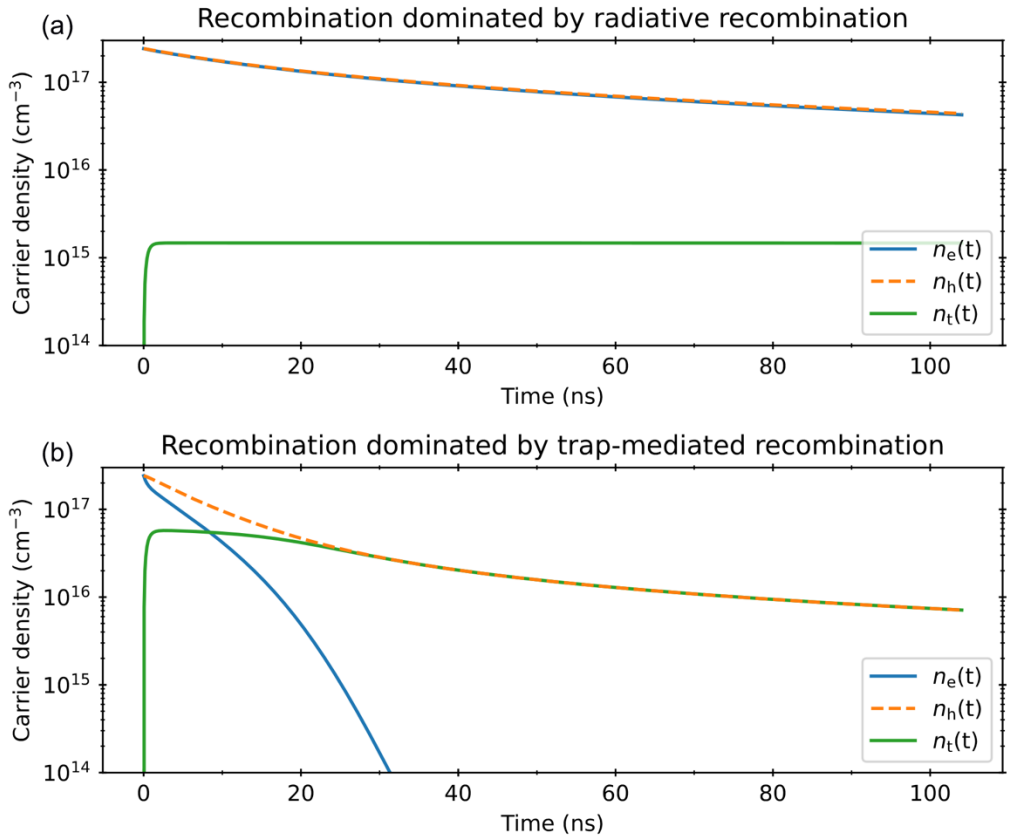

Fig. S11 (a) Simulated temporal evolution of the charge-carrier density in the radiative recombination regime and (b) the trap-mediated recombination regime, based on the model and parameters described in Supplementary Note 2.

We note that the above analysis can be qualitatively captured by the simple ratio of $I_{\mathrm{TRPL}}/{\sigma_{\mathrm{TRMC}}}^2$ without the need to explicitly solve the coupled rate equations. As detailed in the main text, this ratio reflects the relative populations of minority and majority charge carriers. A decrease in $I_{\mathrm{TRPL}}/{\sigma_{\mathrm{TRMC}}}^2$ therefore indicates that the minority carrier density is lower than that of the majority carriers, as clearly demonstrated in Fig. S11b.

We further emphasize that although our discussion has focused on trap-mediated recombination, the ratio $I_{\mathrm{TRPL}}/{\sigma_{\mathrm{TRMC}}}^2$ can in principle probe any charge-selective process, including charge extraction as we demonstrate in the main text.

Supplementary Note 3: Explaining the slight divergence in I_{TRPL} and $\sigma_{\mathrm{TRMC}}{}^2$

The experimental I_{TRPL} and $\sigma_{\mathrm{TRMC}}{}^2$ transients shown in Fig. 1b (main text) for Quartz(Q)/$FA_{0.83}Cs_{0.17}Pb(I_{0.6}Br_{0.4})_3$/PMMA show a slight divergence while maintaining sufficiently long lifetime, suggesting that the simple model presented in Supplementary Note 2 does not completely capture the complex recombination pathways present in metal-halide perovskite.

This effects may arise from an existence of multiple shallow traps, which has recently been demonstrated by Yuan et al.[7] By combining photoluminescence measurements and drift-diffusion modelling, they have shown that a metal halide perovskite may exhibit high density (~ 10^{18} cm^{-3}) of multiple types of electron and hole shallow traps. Therefore, the treatment of trap-assisted recombination may be more complicated than the simple approximation of one type of electron- or hole-only type reported previously.

Therefore, we simulate our TRPL and TRMC transients by employing a set of coupled differential equations that take shallow trapping of both electron and hole into account, as follows:

$$\frac{dn_{\mathrm{e}}(t)}{dt} = -R_{\mathrm{eh}}n_{\mathrm{e}}(t)n_{\mathrm{h}}(t) - R_{\mathrm{pop\_e}}\left(N_{\mathrm{t\_e}} - n_{t\_e}(t)\right)n_{\mathrm{e}}(t) + k_{detrap\_e}n_{t\_e}(t) - R_{depop\_e}n_{t\_e}(t)n_h(t) \quad \text{(S7)}$$

$$\frac{dn_{\mathrm{h}}(t)}{dt} = -R_{\mathrm{eh}}n_{\mathrm{e}}(t)n_{\mathrm{h}}(t) - R_{\mathrm{pop\_h}}\left(N_{\mathrm{t\_h}} - n_{\mathrm{t\_h}}(t)\right)n_{\mathrm{h}}(t) + k_{\mathrm{detrap\_h}}n_{t\_h}(t) - R_{\mathrm{depop\_h}}n_{\mathrm{t\_h}}(t)n_{\mathrm{e}}(t) \quad \text{(S8)}$$

$$\frac{dn_{\mathrm{t\_e}}(t)}{dt} = R_{\mathrm{pop\_e}}\left(N_{\mathrm{t\_e}} - n_{\mathrm{t\_e}}(t)\right)n_{\mathrm{e}}(t) - R_{\mathrm{depop\_e}}n_{\mathrm{t\_e}}(t)n_{\mathrm{h}}(t) - k_{\mathrm{detrap\_e}}n_{\mathrm{t\_e}}(t) \quad \text{(S9)}$$

$$\frac{dn_{\mathrm{t\_h}}(t)}{dt} = R_{\mathrm{pop\_h}}\left(N_{\mathrm{t\_h}} - n_{\mathrm{t\_h}}(t)\right)n_{\mathrm{h}}(t) - R_{\mathrm{depop\_h}}n_{\mathrm{t\_h}}(t)n_{\mathrm{e}}(t) - k_{\mathrm{detrap\_h}}n_{\mathrm{t\_h}}(t) \quad \text{(S10)}$$

where $n_{\mathrm{t\_e}}(t)$, $n_{\mathrm{t\_h}}(t)$, $N_{\mathrm{t\_e}}$, $N_{\mathrm{t\_h}}$ are the trapped electron density, trapped hole density, total electron trap density and total hole trap density respectively. $R_{\mathrm{pop\_e}}$, $R_{\mathrm{pop\_h}}$, $R_{\mathrm{depop\_e}}$, $R_{\mathrm{depop\_h}}$, $k_{\mathrm{detrap\_e}}$, $k_{\mathrm{detrap\_h}}$ are the trap population, depopulation and detrapping rate constants for electrons and holes respectively. $(N_{\mathrm{t}} - n_{\mathrm{t}}(t))$ denotes the unoccupied trap density. Here, we assume that traps are initially unfilled $(n_{\mathrm{t}}(t = 0) = 0)$.

Similar to Supplementary Note 2, Equations S7, S8, S9 and S10 were solved numerically to obtain $n_{\mathrm{e}}(t)$, $n_{\mathrm{h}}(t), n_{\mathrm{t\_e}}(t)$ and $n_{\mathrm{t\_h}}(t)$. Then, I_{TRPL} and $\sigma_{\mathrm{TRMC}}{}^2$ transients were obtained with Equations S5 and S6. The following parameters in Table S4 are used for the simulation.

Table S4 Parameters used for simulating I_{TRPL} and $\sigma_{TRMC}{}^2$ transients by using the model discussed in Supplementary Note 3.

Parameters	Values	Reference
$n_{\mathrm{e}}(\mathrm{t} = 0)$ ($\mathrm{cm^{-3}}$)	2.42×10^{17}	Table S2
n_{h} $(\mathrm{t} = 0)$ ($\mathrm{cm^{-3}}$)	2.42×10^{17}	
$n_{\mathrm{t\_e}}(\mathrm{t} = 0)$ ($\mathrm{cm^{-3}}$)	0	-
$n_{\mathrm{t\_h}}(\mathrm{t} = 0)$ ($\mathrm{cm^{-3}}$)	0	-
μ ($\mathrm{cm^2V^{-1}s^{-1}}$)	24.5	Table S5
R_{eh} ($\mathrm{cm^3s^{-1}}$)	1.54×10^{-10}	Table S7
$N_{\mathrm{t\_e}}$($\mathrm{cm^{-3}}$)	1.64×10^{17}	Simulation
$R_{\mathrm{pop\_e}}$($\mathrm{cm^3s^{-1}}$)	1.51×10^{-10}	Simulation
$R_{\mathrm{depop\_e}}$($\mathrm{cm^{-3}s^{-1}}$)	1.0×10^{-12}	Simulation
$k_{\mathrm{detrap\_e}}$($\mathrm{s^{-1}}$)	7.9×10^{7}	Simulation
$N_{\mathrm{t\_h}}$($\mathrm{cm^{-3}}$)	6.96×10^{15}	Simulation
$R_{\mathrm{pop\_h}}$($\mathrm{cm^3s^{-1}}$)	9.5×10^{-9}	Ref. 1
$R_{\mathrm{depop\_h}}$($\mathrm{cm^{-3}s^{-1}}$)	1.42×10^{-9}	Ref. 1
$k_{\mathrm{detrap\_h}}$($\mathrm{s^{-1}}$)	5.6×10^{4}	Ref. 1

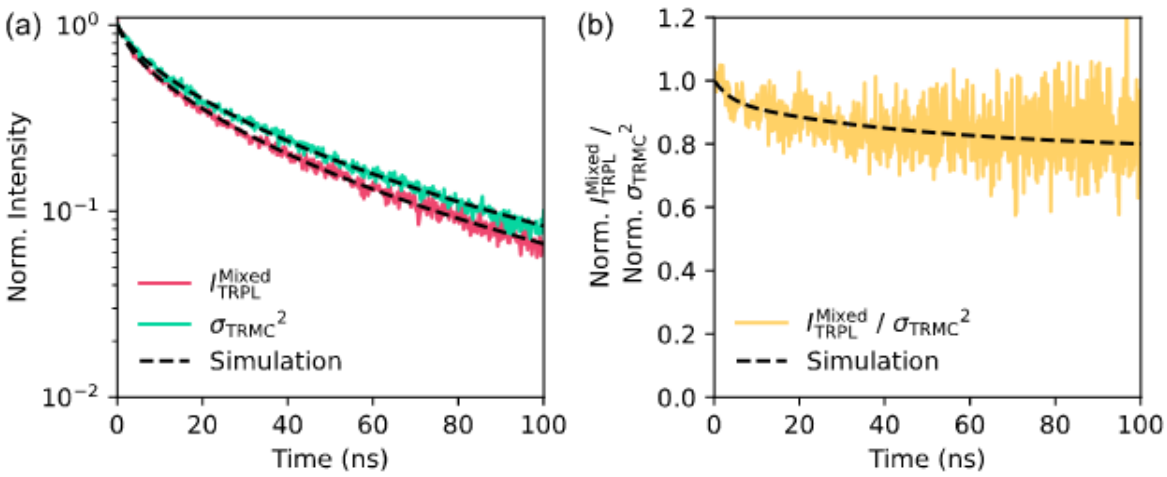

Fig. S12 (a) Mixed-phase TRPL (I_{TRPL}^{Mixed}) and square of the mircrowave photoconductivity ($\sigma_{TRMC}{}^2$) transients of Q/$FA_{0.83}Cs_{0.17}Pb(I_{0.6}Br_{0.4})_3$/PMMA excited with 530 nm wavelength at the fluence of 3.6 μJcm^{-2} with simulated transients obtained from the model discussed in Supplementary Note 3. (b) The ratio of I_{TRPL}^{Mixed} and $\sigma_{TRMC}{}^2$ with the simulation.

Inclusion of the additional shallow traps allows us to describe the long-lived charge-carrier dynamics with the slight divergence in the transient originating from trapping. The early decay in the $I_{\mathrm{TRPL}}^{\mathrm{Mixed}}/\sigma_{\mathrm{TRMC}}{}^2$ ratio arises from the initial charge-carrier trapping, but it is quickly compensated by fast detrapping, mitigating the charge selectivity induced by trapping.

Supplementary Note 4: Charge-carrier funnelling dynamics from the mixed phase to I-rich phase after halide segregation

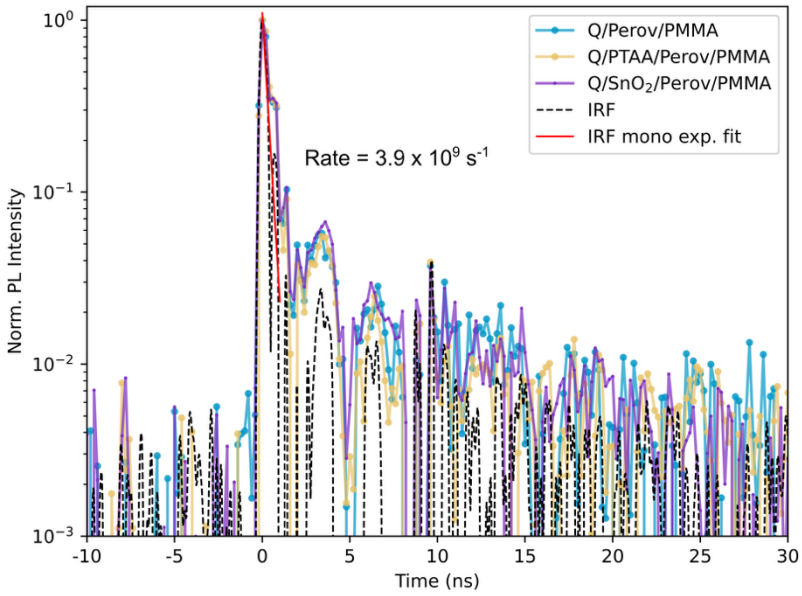

Fig. S13 Normalised mixed-phase TRPL transients after halide segregation with instrument response function (IRF).

Following halide segregation, the mixed-phase TRPL transients become markedly faster and are limited by the instrument response function (IRF), which was determined from the direct exposure of the excitation pulsed laser without the bandpass filter. Thus, irrespective of the presence of a charge-transport layer, charge-carrier funnelling into the I-rich phase dominates and leads to strong quenching of the mixed-phase PL, with the apparent decay constrained by the IRF. This is consistent with previous report that charge-carrier funnelling occurs on a timescale of tens of picoseconds.[8]

Supplementary Note 5: Mobility Calculation from TRMC

The effective electron-hole sum mobility was extracted from the TRMC data using the method illustrated previously by Wehrenfennig *et al*.[9] The sheet photoconductivity ΔS of a thin film between two media of refractive indices n_{A} and n_{B} with its thickness much smaller than the 102 GHz microwave (MW) probe can be expressed as :

$$\Delta S = -\epsilon_0 c(n_{\mathrm{A}} + n_{\mathrm{B}})\left(\frac{\Delta T}{T}\right) \tag{S11}$$

where ϵ_0 is the vacuum permittivity, c is the speed of light and $\Delta T/T$ is the ratio of photo-induced change in the MW electric field to the transmitted MW electric field in the dark. In this study, n_{A} is the refractive index of a z-cut quartz, which is 2.13 and n_{B} is the refractive index of air, which is 1.

Deriving the charge-carrier mobility μ from ΔS requires the knowledge of the number of photo-excited charge-carriers *N*, which can be calculated as:

$$N = \varphi \frac{E\lambda}{hc}\left(1 - R_{\mathrm{pump}} - T_{\mathrm{pump}}\right) \tag{S12}$$

Where φ is the photon-to-charge branching ratio, E is the energy obtained in an optical excitation pulse with wavelength λ, h is the Planck's constant, R_{pump} and T_{pump} are the reflected and transmitted fractions of the pump beam. Then, μ can be calculated with:

$$\mu = \frac{\Delta S A_{\mathrm{eff}}}{Ne} \tag{S13}$$

Here A_{eff} is the effective area of the optical pump.

By using the above equations, the effective mobility $\tilde{\mu} = \varphi\mu$ is expressed as:

$$\varphi\mu = -\epsilon_0 c(n_A + n_B)\frac{A_{eff}hc}{E\lambda e\left(1 - R_{pump} - T_{pump}\right)}\left(\frac{\Delta T}{T}\right) \quad \text{(S14)}$$

In this work, we assume $\varphi = 1$ given that the exciton binding energies are low and free charge-carriers are mostly generated immediately after excitation,[10] but more generally, $\varphi\mu$ is a lower limit. The charge-carrier mobility obtained here is the sum of electron and hole mobilities and they cannot be separated.

To obtain $\varphi\mu$, $\Delta T/T$ at time zero against E was plotted and a linear function was fitted based on Equation S14 across the first four fluences (Table S2) where the linearity is conserved. Then, $\varphi\mu$ was obtained from the gradient.

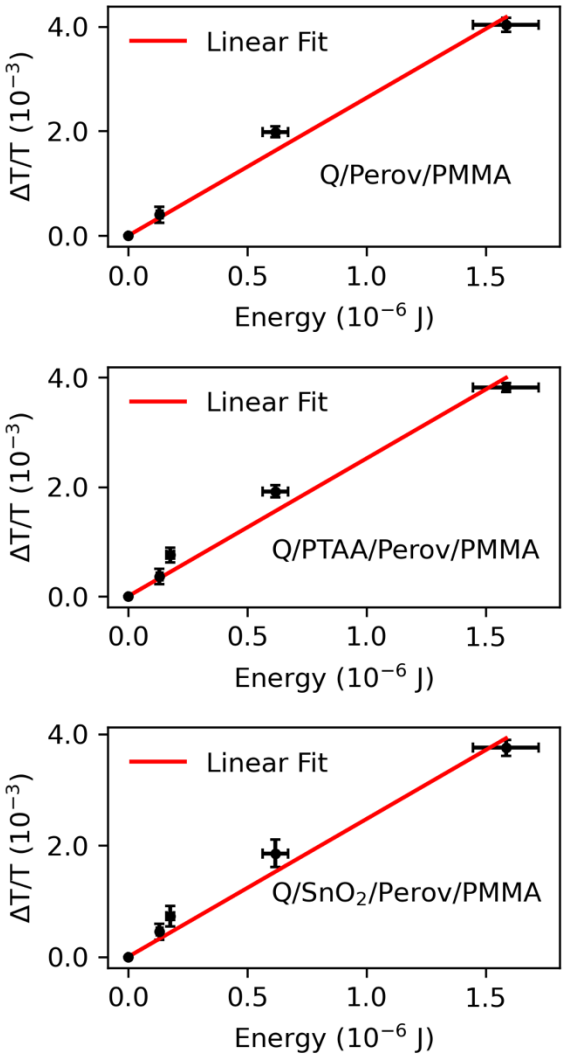

Fig. S14 Linear Fit using Equation S14 to obtain the mobility.

Table S5 Charge-carrier mobilities extracted from Equation S14

Sample	μ ($cm^2V^{-1}s^{-1}$)
Q/Perov/PMMA	24.5 ± 1.2
Q/PTAA/Perov/PMMA	24.2 ± 1.4
Q/SnO_2/Perov/PMMA	23.8 ± 1.4

Supplementary Note 6: Data processing to determine $I_{\mathrm{TRPL}}/{\sigma_{\mathrm{TRMC}}}^2$ ratio.

Reliable evaluation of $I_{\mathrm{TRPL}}/{\sigma_{\mathrm{TRMC}}}^2$ ratio requires consistent normalisation of the individual transient of I_{TRPL} and ${\sigma_{\mathrm{TRMC}}}^2$. The ${\sigma_{\mathrm{TRMC}}}^2$ transient exhibit an initial dip, arising from the AC-coupled (high-pass) response of the GaAs Schottky detector. To avoid this artefact, the analysis was performed only after a cutoff time (t_{cutoff}) defined by an automated algorithm where t_{cutoff} is determined as the first point following the dip at which the signal shows a sustained negative derivative (decreasing) over five consecutive points. The results are shown in Table S6 below.

Table S6 The cutoff time (t_{cutoff}) for the I_{TRPL} and ${\sigma_{TRMC}}^2$ transients before and after halide segregation.

Sample	t_{cutoff} (ns)	
	Before Segregation	After Segregation
Q/Perov/PMMA	3.7	3.4
Q/PTAA/Perov/PMMA	3.3	2.4
Q/SnO_2/Perov/PMMA	3.2	3.4

The t_{cutoff} was subsequently redefined as t = 0 ns. For normalisation, the initial value was obtained by fitting the first 2 ns of the transient with a monoexponential function and taking the fitted amplitude at t = 0 ns as the normalisation factor. This approach minimises errors associated with using a single noise-sensitive point at t = 0 ns. The $I_{\mathrm{TRPL}}/{\sigma_{\mathrm{TRMC}}}^2$ ratio was then calculated by dividing re-normalised I_{TRPL} and ${\sigma_{\mathrm{TRMC}}}^2$ transients. The data processing methods are summarised in the Fig. S15. We note that the $I_{\mathrm{TRPL}}^{\mathrm{I-rich}}$ transients had an oscillatory pulse response originating from the photodetector, particularly at high fluence. To mitigate the noise originating from this, the $I_{\mathrm{TRPL}}^{\mathrm{I-rich}}$ signal was smoothened with a Savitzky-Golay filter prior to calculating the ratio.

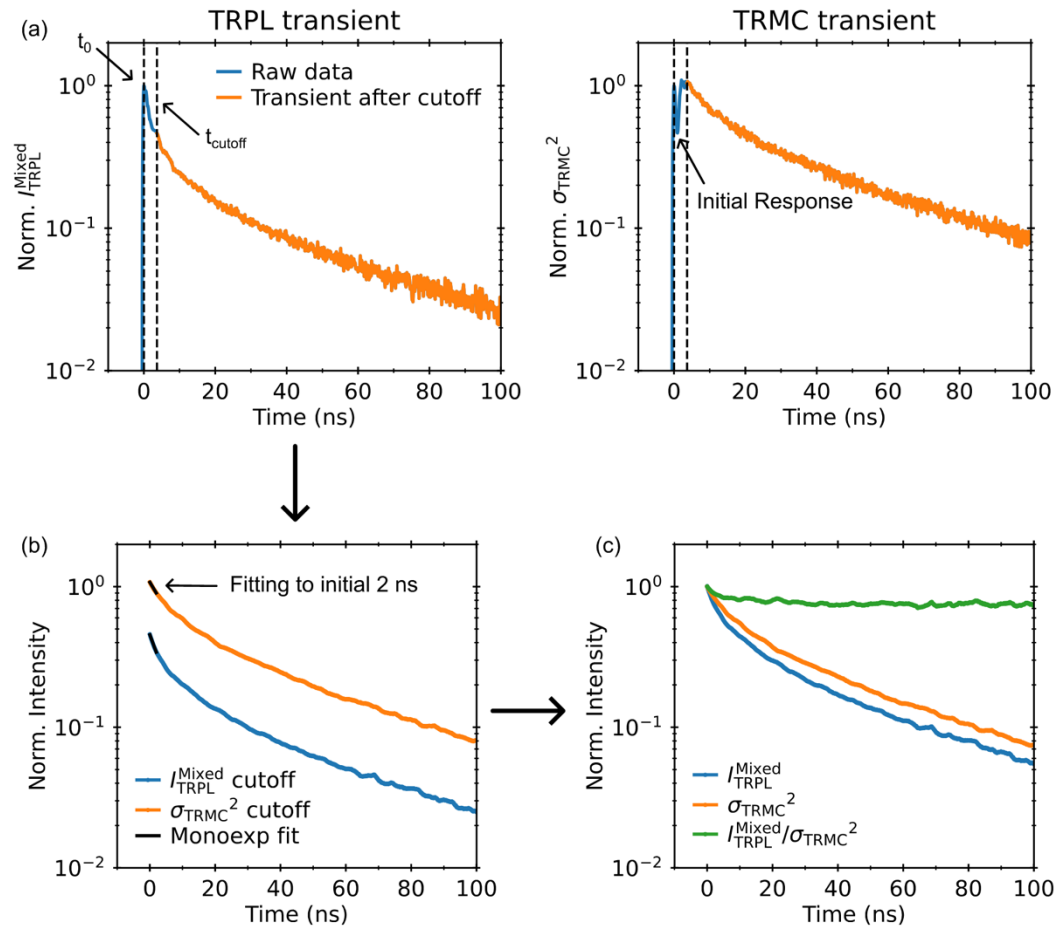

Fig. S15 Workflow for obtaining an accurate $I_{TRPL}/{\sigma_{TRMC}}^2$ ratio. (a) Experimental I_{TRPL} and ${\sigma_{TRMC}}^2$transients of Q/Perov/PMMA excited with a pulsed 530 nm laser at a fluence of 3.6 μJcm^{-2}. t_0 denotes t = 0 ns and t_{cutoff} is the cutoff time determined using the algorithm described in Supplementary Note 6. Only the transient after the cutoff was used to avoid the initial artefact from the GaAs Schottky diode. (b) The transients after t_{cutoff} were fitted with a monoexponential function over the initial 2 ns and the initial amplitude of the fit at t = 0 ns was used as the normalisation factor. (c) The resulting normalised transients and their ratio.

Supplementary Note 7: Trends in the ratio of $I_{\mathrm{TRPL}}^{\mathrm{I-rich}}/{\sigma_{\mathrm{TRMC}}}^2$ after halide segregation

Figs. 3h and i in the main manuscript show that following halide segregation, the charge-carrier imbalance is less pronounced for the half stacks Q/PTAA/Perov/PMMA and Q/SnO_2/Perov/PMMA, as evidenced by the increased amplitude of the slow late-time decay of the ratio of $I_{\mathrm{TRPL}}^{\mathrm{I-rich}}/{\sigma_{\mathrm{TRMC}}}^2$. We attribute this behaviour to enhanced charge-carrier back transfer from charge transport layers to the I-rich phase. The back transfer injects minority charge carriers into the I-rich phase, resulting in a larger increase in $I_{\mathrm{TRPL}}^{\mathrm{I-rich}}$ than in ${\sigma_{\mathrm{TRMC}}}^2$. Photoluminescence scales with the product of majority and minority carrier densities (Equation 2 of the main manuscript) and is therefore more sensitive to the minority carrier population, whereas σ_{TRMC} reflects the sum of both carrier contributions and weights them equally (Equation 1 of the main manuscript). The asymmetric influence of minority-carrier injection results in less pronounced reduction in I_{TRPL} compared to ${\sigma_{\mathrm{TRMC}}}^2$ (Table S6), thereby reducing the divergence between I_{TRPL} and ${\sigma_{\mathrm{TRMC}}}^2$ and increasing the ratio of I_{TRPL} and ${\sigma_{\mathrm{TRMC}}}^2$. This is analogous to case 1 and case 2 described in Equation 3 of the main manuscript, where an increase in minority charge carriers (numerator) leads to an increase in the ratio of I_{TRPL} and ${\sigma_{\mathrm{TRMC}}}^2$. This agrees well with our previous study showing that $FA_{0.83}Cs_{0.17}Pb(I_{1-x}Br_x)_3$ with higher iodide content exhibits stronger hole back transfer from PTAA owing to a more favourable energy-level alignment.[1] However, such an increase in the lifetimes of I_{TRPL} and ${\sigma_{\mathrm{TRMC}}}^2$ transients following halide segregation still competes with enhanced radiative recombination, resulting in an overall decrease in lifetime after segregation, but to a lesser extent than that in the Q/Perov/PMMA thin film.

The reduction in charge-carrier imbalance at later times may also partly originate from charge carriers being generated further away from the interface (based on the Beer-Lambert excitation profile) and therefore being unable to reach the interface owing to the enhanced radiative recombination. However, we estimate such effects to be less significant than those arising from back transfer since the comparably high mobility of the perovskite films will enable homogeneous distribution of charge-carriers along the depth profile to occur within a couple of ns.[11, 12]

Supplementary Note 8: Calculation of diffusion length ratio

The diffusion length of charge carriers L_{D} is defined as:

$$L_{\mathrm{D}} = \sqrt{\frac{\mu k_{\mathrm{b}} T \tau}{e}} \tag{S15}$$

where μ is the charge-carrier mobility and τ is the lifetime of charge-carriers. The ratio of the diffusion length after and before halide segregation $\frac{L_{\mathrm{D\_after}}}{L_{\mathrm{D\_before}}}$ can be expressed as

$$\frac{L_{\mathrm{D\_after}}}{L_{\mathrm{D\_before}}} = \sqrt{\frac{\mu_{\mathrm{after}} \tau_{\mathrm{after}}}{\mu_{\mathrm{before}} \tau_{\mathrm{before}}}} \tag{S16}$$

where μ_{after} and μ_{before} are the mobility after and before halide segregation. τ_{after} and τ_{before} are lifetimes after and before halide segregation. The ratio of $\frac{\mu_{\mathrm{after}}}{\mu_{\mathrm{before}}}$ are obtained from the initial intensity (t = 0 ns) of the σ_{TRMC} transient at the illumination time of 6 hr and 0 hr respectively. The lifetimes are average lifetimes obtained from stretched-exponential fits to the $I_{\mathrm{TRPL}}$and σ_{TRMC} transients. The final ratio of $\frac{L_{\mathrm{D\_after}}}{L_{\mathrm{D\_before}}}$ is calculated by taking the average of L_{D} obtained from each transient. The results are shown in the Table 9 below, with the last column showing a $\frac{L_{\mathrm{D\_after}}}{L_{\mathrm{D\_before}}}$ ratio of approximately 65%, i.e. an approximate 35% reduction in charge-carrier diffusion length following halide segregation.

Table S6 Ratio of mobility μ_{after}/μ_{before}, lifetime $\tau_{after}/\tau_{before}$ for TRPL and TRMC and the resulting average diffusion length L_{D_after}/L_{D_before} for Q/Perov/PMMA, Q/PTAA/Perov/PMMA and Q/SnO_2/Perov/PMMA after and before halide segregation

Sample	$\frac{\mu_{\text{after}}}{\mu_{\text{before}}}$	$\frac{\tau_{\text{after}}}{\tau_{\text{before}}}$ from I_{TRPL}	$\frac{\tau_{\text{after}}}{\tau_{\text{before}}}$ from σ_{TRMC}	$\frac{L_{\text{D\_after}}}{L_{\text{D\_before}}}$
Q/Perov/PMMA	0.81	0.55	0.53	0.662 ± 0.004
Q/PTAA/Perov/PMMA	0.50	0.80	0.69	0.61 ± 0.02
Q/SnO_2/Perov/PMMA	0.72	0.87	0.65	0.74 ± 0.05

Compared to the neat perovskite film, the degree of mobility preservation upon halide segregation decreases somewhat in the presence of charge transport layers, yielding 72 % and 50 % mobility retention for Q/PTAA/Perov/PMMA and Q/SnO_2/Perov/PMMA respectively (Table S6). This additional reduction in mobility likely originates from external factors associated with the perovskite/charge transport layer interface, as the value of the electron-hole sum mobility does not decline with halide segregation as severely when no transport layers are present. These findings suggest that the presence of CTLs results in an increasing number of scattering sites for free-charge carriers following halide segregation. We postulate that upon halide segregation, the rearrangement of halide ions may disrupt the interfacial bonding between perovskite and charge transport layers, thereby introducing additional interfacial defects that serve as charge-carrier scattering sites.

Supplementary Note 9: Calculating change in the quasi-Fermi level splitting

Halide segregation leads to a pronounced increase in PL intensity while simultaneously shortening charge-carrier lifetime (Fig. 3 in the main manuscript), indicating that the enhanced PL arises primarily from increased radiative recombination. The PL intensity is proportional to the product of the radiative rate constant (R_{eh}) and the electron and hole densities (n_{e} and n_{h}). Given that R_{eh} decreases with increasing iodide content in $FA_{0.83}CS_{0.17}Pb(I_{1-x}Br_x)_3$,[1] the observed increase in PL intensity likely stems from an increase in local charge-carrier density owing to funnelling into the I-rich domains, which occupy only a small fraction of the perovskite volume.

The photoluminescence quantum yield (*PLQY*), defined as the ratio of emitted to absorbed photons, allows us to estimate the change in quasi-Fermi level splitting ($\Delta QFLS$) owing to the increase in PL intensity, which is closely related to open-circuit voltage, as following:

$$\Delta QFLS = QFLS_{\mathrm{rad}}^{\mathrm{after}} - QFLS_{\mathrm{rad}}^{\mathrm{before}} + k_b T \ln\left(\frac{PLQY_{\mathrm{after}}}{PLQY_{\mathrm{before}}}\right) \quad \text{(S17)}$$

where k_b is the Boltzmann constant, T is the temperature, $QFLS_{\mathrm{rad}}^{\mathrm{after}}$ and $QFLS_{\mathrm{rad}}^{\mathrm{before}}$ are the radiative limits of the I-rich phase after segregation and mixed phase before segregation respectively, which set the maximum achievable splitting, and $PLQY_{\mathrm{after}}$ and $PLQY_{\mathrm{before}}$ are the *PLQY* of the I-rich phase after segregation and mixed phase before segregation respectively. Given that charge-carrier funnel into the I-rich phase within < 1 ns (see Fig. S13) before significant recombination in the mixed phase, we assume that charge-carriers are effectively absorbed and emitted by the single I-rich phase, preserving the assumption of the detailed balance theory.[13]

Evolution of the narrower bandgap upon segregation lowers $QFLS_{\mathrm{rad}}^{\mathrm{after}}$ compared to $QFLS_{\mathrm{rad}}^{\mathrm{before}}$, leading to the overall decrease in $QFLS$. However, such decrease is compensated by the increase in the PL after segregation. Such $QFLS$ gain is calculated with the last term of Equation S17.

To calculate the relative change in PLQY, we convert the PL spectra (corrected for spectral response by referencing to the known emissivity spectrum of a tungsten filament lamp, with

spectral response in irradiance units, $Wnm^{-1}cm^{-2}$) into photon flux (Φ) by dividing by photon energy. Integration over wavelength yields the total emitted photon flux density N_{em}. The ratio of N_{em} after and before halide segregation gives the relative change in PLQY, given that absorption at 532 nm excitation wavelength remains nearly constant during halide segregation (Fig. 2b and Figs. S4-S5). The results are shown in Table S7 below.

Table S7 Change in the PLQY before and after halide segregation and the resulting gain in quasi-Fermi level splitting (QFLS).

Samples	$PLQY_{after}/PLQY_{before}$	QFLS gain (meV)
Q/Perov/PMMA	2.61	24.8
Q/PTAA/Perov/PMMA	7.54	52.2
Q/SnO_2/Perov/PMMA	1.58	11.9

The slight difference in the change of the photoluminescence intensity before and after halide segregation in the presence of charge transport layers may originate from the additional charge transfer and back transfer mechanisms involved, as discussed further in the main manuscript and Supplementary Note 7.[14]

We note that the $QFLS$ gain shown in Table S7 is substantially smaller than the ~ 200 meV red-shift in the PL peak energies upon halide segregation, suggesting that the enhanced radiative recombination is insufficient to provide significant V_{OC} compensation. Consequently, halide segregation is expected to result in a net loss in V_{OC}, consistent with resports in literature.[15, 16]

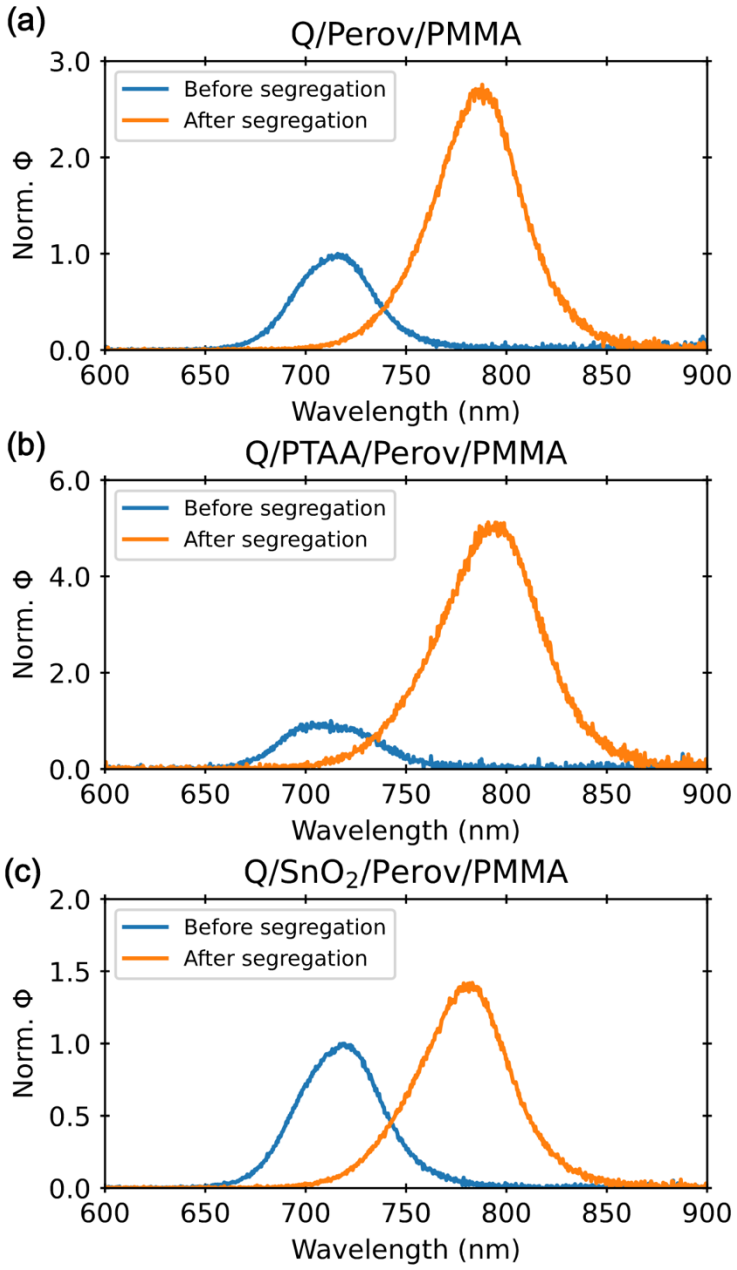

Fig. S16 Normalised photon flux for (a) Q/$FA_{0.83}Cs_{0.17}Pb(I_{0.6}Br_{0.4})_3$ (Perov)/PMMA, (b) Q/PTAA/ Perov/PMMA and (c) Q/SnO_2/Perov/PMMA before and after halide segregation.

Supplementary Note 10: Bimolecular radiative recombination constant from OPTP

Our Optical-pump Terahertz-probe (OPTP) spectroscopy setup[9, 17] uses a Spectra Physics Mai Tai-Ascend-Spitfire Pro Ti:Sapphire regenerative amplifier. The amplifier generates an ultra-fast laser with 35 fs pulse duration, 800 nm centre wavelength and 5 kHz repetition rate. An optical pump excitation wavelength of 530 nm was achieved by using a Traveling-wave Optical Parametric Amplifier of Superfluorescence (TOPAS) with a sum-frequency generation of the signal pulse. THz probe pulses were generated with a spintronic emitter which consists of 1.9 nm Tungsten/2.0 nm $Co_{40}Fe_{40}Be_{20}$/1.9 nm Platinum coated with anti-reflectivity and high-reflectivity coatings[18]. The sample stored in an evacuated chamber at pressure less than 10^{-1} mbar was excited with the pump and probed with the THz pulse shortly after. The pump and THz pulses were chopped with optical choppers with frequencies of 1.25 and 2.5 kHz respectively to obtain the THz transmission change ΔT. The sigma of pump and probe beam at the sample positions were measured as 1.75 mm and 0.33 mm respectively. The power of the pump pulses was tuned by a ND filter wheel. The THz transmission from thin films was detected by electro-optic sampling in a (110)-ZnTe crystal (1 mm thickness) with a spatially and temporally overlapping 800 nm gate pulse. The THz transmission was measured at the peak of the THz pulse for different delays of the pump beam, mapping the THz transmission as a function of time after photoexcitation.

Under pulsed excitation, minimal halide segregation is induced, causing additional charge selective processes as discussed in Supplementary Note 3. The presence of multiple pathways complicates the extraction of a fluence-dependent R_{eh} parameter from TRMC/TRPL measurements. OPTP spectroscopy provides access to earlier timescales (< 1 ns), enabling these effects to be minimized. The well-established k_{nonrad}, R_{eh}, R_{Auger} model was used[19].

$$\frac{dn}{dt} = -k_{\mathrm{nonrad}}n - R_{\mathrm{eh}}n^2 - R_{\mathrm{Auger}}n^3 \tag{S18}$$

Where n is the charge-carrier density, k_{nonrad} is the monomolecular recombination constant, and R_{eh} is the bimolecular recombination constant, and R_{Auger} is the Auger recombination constant.

Equation S18 is first solved in terms of the experimentally observed quantity $x(t) = \Delta T/T$, which is the photoinduced change in THz transmission. $x(t)$ is proportional to $n(t)$ with the following relationship:

$$n(t)^i = \varphi^{i-1} C^{i-1} x(t)^i \tag{S19}$$

where i is the recombination order, φ is the photon-to-charge branching ratio, $C = n_0/x(0)$ is the proportionality factor between the immediate THz response at $t = 0$ and the absorbed photon density n_0.

By substituting Equation S19 into Equation S18, Equation S18 can be written as :

$$\frac{dx(t)}{dt} = -k_{\text{nonrad}} x(t) - R_{\text{eh}} \varphi C x(t)^2 - R_{\text{Auger}} \varphi^2 C^2 x(t)^3 \tag{S20}$$

The numerical solutions to this ODE are fitted globally to the decays using the least squares method across all fluences in order to extract φR_{eh}. Given that $0 \leq \varphi \leq 1$, the values presented for R_{eh} reported here are underestimates for the true intrinsic values.

In order to account for an initially spatially varying charge-carrier density (due to absorption following the Beer-Lambert law), the fitting algorithm takes into account an exponentially decaying charge-carrier density. This is done by dividing the film into 30 equally thick slices and computing the decay function for each of these individually.

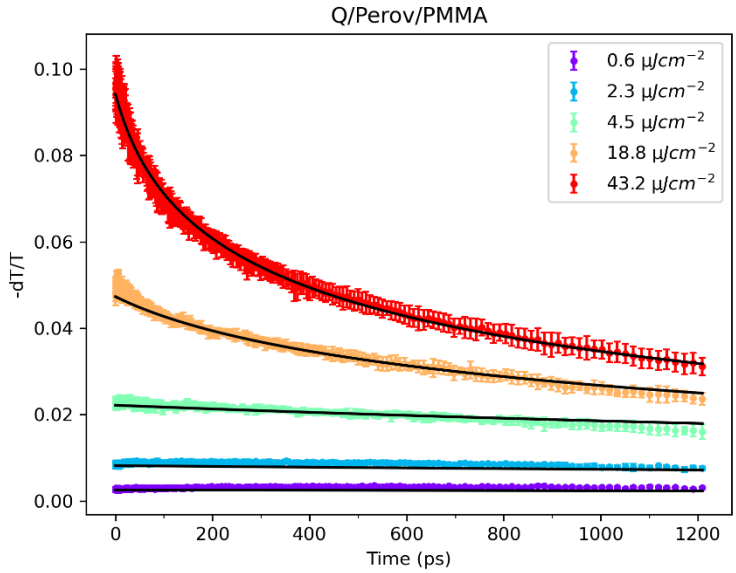

Fig. S17 Fluence-dependent OPTP transients of Q/Perov/PMMA with best fit of Equation S20

Table S7 Extracted parameters from Equation S20 for Q/Perov/PMMA

Parameters	Values
k_{nonrad} (s^{-1})	4.63×10^{7}
R_{eh} ($cm^{3}s^{-1}$)	1.54×10^{-10}
R_{Auger}($cm^{6}s^{-1}$)	4.4×10^{-29}

References

1. J. E. Lee, S. G. Motti, R. D. J. Oliver, S. Yan, H. J. Snaith, M. B. Johnston and L. M. Herz, *Adv. Funct. Mater.*, 2024, **34**, 2401052.
2. K. A. Elmestekawy, A. D. Wright, K. B. Lohmann, J. Borchert, M. B. Johnston and L. M. Herz, *ACS Nano*, 2022, **16**, 9640-9650.
3. D. Nečas and P. Klapetek, 2012, **10**, 181-188.
4. T. Leijtens, G. E. Eperon, A. J. Barker, G. Grancini, W. Zhang, J. M. Ball, A. R. S. Kandada, H. J. Snaith and A. Petrozza, *Energy Environ. Sci.*, 2016, **9**, 3472-3481.
5. G.-J. A. H. Wetzelaer, M. Scheepers, A. M. Sempere, C. Momblona, J. Ávila and H. J. Bolink, *Adv. Mater.*, 2015, **27**, 1837-1841.
6. D. Meggiolaro, S. G. Motti, E. Mosconi, A. J. Barker, J. Ball, C. Andrea Riccardo Perini, F. Deschler, A. Petrozza and F. De Angelis, *Energy Environ. Sci.*, 2018, **11**, 702-713.
7. Y. Yuan, G. Yan, C. Dreessen, T. Rudolph, M. Hülsbeck, B. Klingebiel, J. Ye, U. Rau and T. Kirchartz, *Nat. Mater.*, 2024, **23**, 391-397.
8. S. G. Motti, J. B. Patel, R. D. J. Oliver, H. J. Snaith, M. B. Johnston and L. M. Herz, *Nat. Commun.*, 2021, **12**, 6955.
9. C. Wehrenfennig, M. Liu, H. J. Snaith, M. B. Johnston and L. M. Herz, *Energy Environ. Sci.*, 2014, **7**, 2269.
10. A. Miyata, A. Mitioglu, P. Plochocka, O. Portugall, J. T.-W. Wang, S. D. Stranks, H. J. Snaith and R. J. Nicholas, *Nat. Phys.*, 2015, **11**, 582-587.
11. C. L. Davies, M. R. Filip, J. B. Patel, T. W. Crothers, C. Verdi, A. D. Wright, R. L. Milot, F. Giustino, M. B. Johnston and L. M. Herz, *Nat. Commun.*, 2018, **9**, 293.
12. J. E. Lee, M. Righetto, B. W. J. Putland, S. Yan, J. R. S. Lilly, S. Lal, H. Jin, N. K. Noel, M. B. Johnston, H. J. Snaith and L. M. Herz, *ACS Appl. Mater. Interfaces*, 2025, **17**, 40363-40374.
13. P. Caprioglio, S. Caicedo-Dávila, T. C.-J. Yang, C. M. Wolff, F. Peña-Camargo, P. Fiala, B. Rech, C. Ballif, D. Abou-Ras, M. Stolterfoht, S. Albrecht, Q. Jeangros and D. Neher, *ACS Energy Lett.*, 2021, **6**, 419-428.
14. V. J.-Y. Lim, A. J. Knight, R. D. J. Oliver, H. J. Snaith, M. B. Johnston and L. M. Herz, *Adv. Funct. Mater.*, 2022, **32**, 2204825.
15. S. Mahesh, J. M. Ball, R. D. J. Oliver, D. P. McMeekin, P. K. Nayak, M. B. Johnston and H. J. Snaith, *Energy Environ. Sci.*, 2020, **13**, 258.
16. L. Du, F. Cao, R. Meng, Y. Zhang, J. Zhang, Z. Gao, C. Chen, C. Li, D. Zhao, J. Ye, Z. Li and C. Xiao, *Nat. Commun.*, 2025, **16**, 8080.
17. P. Tiwana, P. Parkinson, M. B. Johnston, H. J. Snaith and L. M. Herz, *J. Phys. Chem. C*, 2010, **114**, 1365-1371.
18. F. M. Wagner, S. Melnikas, J. Cramer, D. A. Damry, C. Q. Xia, K. Peng, G. Jakob, M. Kläui, S. Kičas and M. B. Johnston, *J. Infrared Millim. Terahertz Waves*, 2023, **44**, 52-65.
19. L. M. Herz, *Rev. Phys. Chem.*, 2016, **67**, 65-89.